Fluorescence spectrum and charge state control of divacancy qubits via illumination at elevated temperatures in 4*H* silicon carbide

A. Csóré,[1] I. G. Ivanov,[2] N. T. Son ⬤,[2] and A. Gali ⬤[1,3]

[1]*Department of Atomic Physics, Budapest University of Technology and Economics, Budafoki út 8., Budapest H-1111, Hungary*
[2]*Department of Physics, Chemistry and Biology, Linköping University, SE-58183 Linköping, Sweden*
[3]*Wigner Research Centre for Physics, P.O. Box 49, Budapest H-1525, Hungary*

Divacancy in its neutral charge state ($V_C V_{Si}^0$) in 4H silicon carbide (SiC) is a leading quantum bit (qubit) contender. Owing to the lattice structure of 4H SiC, four different $V_C V_{Si}$ configurations can be formed. The ground and the optically accessible excited states of $V_C V_{Si}^0$ configurations exhibit a high-spin state, and the corresponding optical transition energies are around ≈ 1.1 eV falling in the near-infrared wavelength region. Recently, photoluminescence (PL) quenching has been experimentally observed for all $V_C V_{Si}$ configurations in 4H SiC at cryogenic temperatures. It has been shown that $V_C V_{Si}^0$ is converted to $V_C V_{Si}^-$ and it remains in this shelving dark state at cryogenic temperatures until photoexcitation with the threshold energies or above is applied to convert $V_C V_{Si}^-$ back to $V_C V_{Si}^0$. In this study, we demonstrate both in experiments and theory that the threshold energy for reionization is temperature dependent. We carry out density functional theory (DFT) calculations in order to investigate the temperature dependent reionization spectrum, i.e., the spectrum of the $V_C V_{Si}^- \rightarrow V_C V_{Si}^0$ process. We find that simultaneous optical reionization and qubit manipulation can be carried out at room temperature with photoexcitation at the typical excitation wavelength used for readout of the divacancy qubits in 4H SiC, in agreement with our experimental data. We also provide the analysis of the PL spectrum of $V_C V_{Si}^0$, characteristic for each $V_C V_{Si}^0$ configuration in 4H SiC, using the Huang-Rhys theory, and find that one configuration in 4H SiC stands out in terms of the strength of coherent emission among the four configurations.

I. INTRODUCTION

Spin active point defects in wide band gap semiconductors have proven to be promising candidates for numerous applications in the rapidly emerging field of quantum technology. Leading contender of this family is the negatively charged nitrogen-vacancy defect, i.e., the NV center in diamond with exhibiting many desirable magneto-optical properties [1,2]. Nevertheless, further alternative point defect color centers have been searched for in the past decade embedded in technologically more mature materials than diamond.

A suitable host candidate to this end is silicon carbide (SiC) introducing different crystal modifications called polytypes. The technologically most relevant polytype is the hexagonal 4H SiC which hosts different types of quantum bits (qubits) [3–7] being pivotal in quantum information processing [8–12], ultrasensitive nanosensors in magnetometry [13–18] or thermometry [14,19].

Divacancy is one of the most successful qubits in 4H SiC [3,20] which consists of neighbor carbon and silicon vacancies, $V_C V_{Si}$. 4H SiC consists of Si-C bilayers exhibiting hexagonal (*h*) or quasicubic (*k*) sites. Consequently, $V_C V_{Si}$ possesses four different defect configurations in 4H SiC because of the two possible defect sites for both V_C and V_{Si}. Henceforward, we denote the different configurations with the lattice sites' labels of the C and Si vacancies, respectively, such as $V_C V_{Si}(hh)$, $V_C V_{Si}(kk)$, $V_C V_{Si}(hk)$, and $V_C V_{Si}(kh)$.

The *hh* and *kk* configurations are called axial or on-axis configurations exhibiting C_{3v} symmetry, while the *hk* and *kh* configurations are basal or off-axis configurations with C_{1h} symmetry. Lattice structure of 4H SiC and the $V_C V_{Si}$ defect configurations are shown in Fig. 1.

The divacancy in 4H SiC exhibits several desirable magneto-optical properties making it a promising qubit. In particular, electronic structure of the neutral $V_C V_{Si}$ center ($V_C V_{Si}^0$) introduces high-spin ($S = 1$) ground and optically accessible excited states [3,21–23]. The corresponding no-phonon optical transitions, i.e., the zero-phonon lines (ZPLs) are around 1100 nm falling into the near-infrared (NIR) region where optical fibers and organic tissues have relatively low absorption window. This property makes the divacancy a promising candidate as a single photon emitter with quantum memory for quantum communication and as an ultrasensitive biomarker [24–26]. Indeed, high-fidelity infrared spin-photon interface [27] and entanglement and control of single nuclear spins [28] have been demonstrated with divacancies in 4H SiC. The ZPLs are now labeled [3] and identified with the corresponding configurations [29] as PL1 - $V_C V_{Si}(hh)$, PL2 - $V_C V_{Si}(kk)$, PL3 - $V_C V_{Si}(hk)$, and PL4 - $V_C V_{Si}(kh)$ that were previously labeled as UD2 centers in 4H SiC in the literature [21].

The charge state control of defect qubits is indispensable for robust quantum information processing [30]. Photoexcitation of target point defect qubits may lead to their unwanted
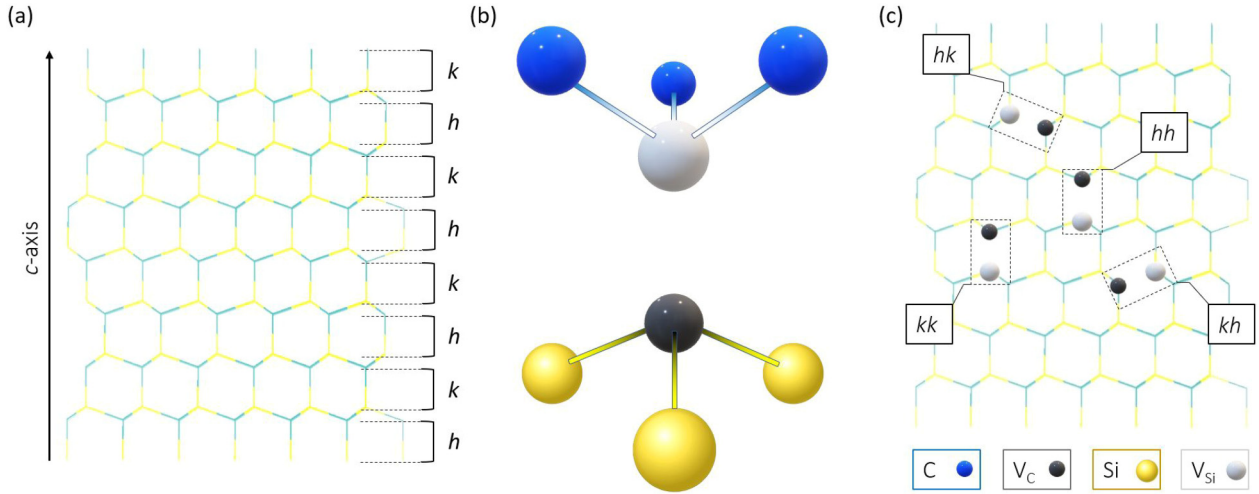
FIG. 1. (a) Lattice structure of 4H SiC. The [0001] crystal axis (*c* axis) and the *h*/*k* bilayers are depicted. (b) Microscopic structure of the divacancy defect. (c) The four possible $V_C V_{Si}$ configurations embedded into 4H SiC. Color code of the atoms and the vacant sites is indicated.

charge switching with losing the qubit state. According to previous *ab initio* studies [31–34], all the divacancy configurations could appear in the positive, neutral, negative, and double negative charge states depending on the position of the Fermi level in 4H SiC which may be actively controlled by doping and electrical switching in a 4H SiC diode [35]. Nevertheless, photoexcitation of the neutral divacancies may lead to the ionization of the defect. Indeed, photoluminescence (PL) quenching of divacancy defects in 4H SiC has been recently observed, i.e., the PL signals of $V_C V_{Si}^0$ defects do not appear upon certain excitation energies [34,36–38]. On the other hand, it has been demonstrated that applying a second laser (repump laser) with a higher photon energy completely recovers the PL intensity of the $V_C V_{Si}^0$ centers [34,36–38]. Here, we note that the PL quenching phenomenon is not unique for $V_C V_{Si}^0$ in 4H SiC but was observed for several other defects (e.g., see Ref. [2] and references therein for NV center in diamond). The physical mechanism behind the quenching phenomenon may be the charge state switching of the corresponding defect upon illumination as already demonstrated by previous experimental and theoretical works [34,36–39]. In this case, the role of the repump laser is to reionize the defect, i.e., to maintain the neutral charge state. In particular, the "dark" charge state has been attributed to either the singly positive [38] or the singly negative charge state [37] of divacancies by earlier experimental works. In order to unravel this issue, we carried out a combined experimental and density functional theory (DFT) study [34] and found that the singly negative charge state $[V_C V_{Si}^-]$ is the dark state because the calculated and observed photoexcitation threshold energies at cryogenic temperatures agreed well for this charge state for all the divacancy configurations in 4H SiC.

In this work, we investigate the temperature dependent charge state control of the $V_C V_{Si}^0$ defect configurations in 4H SiC. To this end, we calculate the $V_C V_{Si}^0$-related PL lineshape and the $V_C V_{Si}^- \rightarrow V_C V_{Si}^0$ reionization spectra based on the Huang-Rhys (HR) theory [40–42], and monitor the appearance of the divacancy PL spectra as a function of the applied repump laser's wavelength and temperature in high-purity semi-insulating 4H SiC samples. We find an ex-

citation scheme with simultaneous charge state control and qubit manipulation of $V_C V_{Si}^0$ by a single color laser beam at elevated temperatures. Our paper is organized as follows: we describe the computational methodology in Sec. II, where we briefly describe the HR theory in Sec. II A, the temperature dependence of the charge transition levels in Sec. II B and the methodology of the *ab initio* DFT calculations in Sec. II C. We report and discuss our results in Sec. III. In particular, PL spectra at cryogenic temperature of the $V_C V_{Si}^0$ defect configurations are discussed in Sec. III A, the simulated $V_C V_{Si}^- \rightarrow V_C V_{Si}^0$ temperature dependent reionization spectra are reported within various levels of approximation in Secs. III B and III C. The experimental data are presented and interpreted by our DFT simulations in Sec. III D. We conclude our work in Sec. IV.

II. METHODOLOGY

A. Huang-Rhys theory

The PL spectrum $[I^{EM}(\hbar\omega)]$ within HR theory can be expressed as [41]

$$I^{EM}(\hbar\omega) = C^{EM}\omega^3 \mu_{EG}^2 \sum_{n,m} c_m(T) \left| \left\langle \Theta_{ES}^m(Q) \middle| \Theta_{GS}^n(Q) \right\rangle \right|^2$$
$$\times \delta\left(E_{ES}^m - E_{GS}^n - \hbar\omega\right), \quad (1)$$

where the transitions from the corresponding vibronic substates of the excited state (ES), indexed by m, to those of the ground state (GS) with the index n are also considered establishing the phonon sideband (PSB) besides the ZPL, i.e., $m = n = 0$ in $I^{EM}(\hbar\omega)$ yields the intensity of ZPL. Generalized coordinate Q appears in both the ES and GS vibrational function Θ according to the HR theory. The temperature dependence appears by the factor $c_m(T)$ with temperature T which will be defined later. In Eq. (1), μ_{EG} is the corresponding matrix element (which is now a three component vector with the length of μ_{EG}) of the transition dipole moment operator, $\hat{\mu}_{EG} = q \sum_j \hat{r}_j$ defined as

$$\mu_{EG} = \langle \Psi_{ES}(r_i) | \hat{\mu}_{EG} | \Psi_{GS}(r_i) \rangle \quad (2)$$

and $\hbar\omega$ is the photon energy. The prefactor ω^3 in Eq. (1) consists of the photon density of states (DOS) causing spontaneous emission ($\sim\omega^2$) and the perturbing field of those photons ($\sim\omega$). In contrast, the absorption spectrum is a linear function of ω since no spontaneous emission is involved. Thus the absorption spectrum can be expressed as

$$I^{\text{ABS}}(\hbar\omega) = C^{\text{ABS}}\mu_{\text{EG}}^2\omega \sum_{n,m} c_n(T)\left|\langle\Theta_{\text{GS}}^n(Q)|\Theta_{\text{ES}}^m(Q)\rangle\right|^2$$
$$\times\, \delta\big(E_{\text{ES}}^m - E_{\text{GS}}^n - \hbar\omega\big), \qquad (3)$$

where C^{EM} and C^{ABS} are the corresponding material and measurement dependent constants of the emission and absorption in Eqs. (1) and (3), respectively. Since $C^{\text{EM/ABS}}$ and $\hat{\mu}_{\text{EG}}$ are constants across the spectrum, we used Eqs. (4) and (5) as the luminescence and absorption line shapes [$L^{\text{EM/ABS}}(\hbar\omega)$], respectively, defined as

$$L^{\text{EM}}(\hbar\omega) = \omega^3 \sum_{n,m} c_m(T)\left|\langle\Theta_{\text{GS}}^{n=0}(Q)|\Theta_{\text{ES}}^m(Q)\rangle\right|^2$$
$$\times\, \delta\big(E_{\text{ES}}^m - E_{\text{GS}}^n - \hbar\omega\big) \qquad (4)$$

and

$$L^{\text{ABS}}(\hbar\omega) = \omega \sum_{n,m} c_n(T)\left|\langle\Theta_{\text{GS}}^n(Q)|\Theta_{\text{ES}}^m(Q)\rangle\right|^2$$
$$\times\, \delta\big(E_{\text{ES}}^m - E_{\text{GS}}^n - \hbar\omega\big). \qquad (5)$$

The vibrational overlap integral can be calculated by applying the HR theory [40] as implemented previously [42]. In the HR framework, three basic assumptions are used: (i) the normal modes, (ii) the vibrational frequencies are identical in the initial and final electronic states, and (iii) the equilibrium configuration is shifted by $\Delta\mathbf{Y}$ in the final state with respect to the initial nuclear configuration. Generalized nuclear configuration weighted by the nuclear masses ($\mathbf{Y}$) can be defined as $\mathbf{Y} = \mathbf{M}^{\frac{1}{2}}\mathbf{X}$, where $\mathbf{X} = (\mathbf{R}_1, \ldots, \mathbf{R}_N) = (X_1, Y_1, Z_1, \ldots, X_N, Y_N, Z_N)$ is a vector constructed by the nuclear coordinates and

$$\mathbf{M} = \begin{bmatrix} M_1 & & & & & \\ & M_1 & & & & \\ & & M_1 & & & \\ & & & M_2 & & \\ & & & & \ddots & \\ & & & & & M_N \end{bmatrix} \qquad (6)$$

is the mass tensor. The partial HR factor (S_k) can be calculated as the scalar product of the normal vectors of mode k ($\mathbf{Y}_0^k$) and the displacement vector of $\Delta\mathbf{Y}$ as

$$S_k = \left(\Delta\mathbf{Y}^{\text{T}}\mathbf{Y}_0^k\right)^2. \qquad (7)$$

The (total) HR factor (S) can be defined as the sum of the partial ones,

$$S = \sum_k^{3N-6} S_k. \qquad (8)$$

While the partial HR factor indicates the weight of phonon mode k in the corresponding electronic transition, total HR factor gives a measure for the strength of the overall electron-phonon coupling. By using the HR factors, overlapping integral of the initial and final vibrational wave functions describing the line shape of the spectrum can be written as

$$\langle\Theta_{\text{f}}^m(Q)|\Theta_{\text{i}}^n(Q)\rangle = \prod_k \langle m_k|n_k\rangle, \qquad (9)$$

where $\Theta_{\text{i}}^n(Q)$ and $\Theta_{\text{f}}^m(Q)$ stand for the vibrational wave functions of the initial and final states, respectively m_k and n_k stand for the phonon occupation of mode k in the final and initial states with the corresponding n and m quantum numbers, respectively, and

$$|\langle m_k|n_k\rangle| = e^{-S_k}\frac{S_k^{m-n}}{(m-n)!}. \qquad (10)$$

At $T = 0$ K, the lowest energy phonon state is occupied in the electronic excited state in the PL process, i.e., $m = 0$. As the temperature raised higher energy m phonon states are occupied. Boltzmann distribution function may be applied at a given temperature for calculating the occupation of ω_k phonon state which is given by $c_m(T)$ in Eqs. (1) and (4). By defining ε as the vibronic excited state's (m) energy in the electronic excited state,

$$\varepsilon_m = E_{\text{ES}}^m - E_{\text{ES}}^0, \qquad (11)$$

$c_m(T)$ can be given as

$$c_m = \frac{\exp\left(\frac{-\varepsilon_m}{k_BT}\right)}{\sum_m \exp\left(\frac{-\varepsilon_m}{k_BT}\right)}. \qquad (12)$$

By this way, the temperature dependent PL line shape may be obtained. In the case of absorption spectrum, $c_n(T)$ can be defined analogously to $c_m(T)$ but it rather represents the occupation of the vibronic excites state in the electronic ground state. We note that all HR spectra presented in this work are normalized.

Experimental determination of the S factor can be carried out via the so-called Debye-Waller (DW) factor (w) [43,44] which can be directly read out from the corresponding spectra. DW factor represents the ratio of the ZPL and total intensity in the corresponding spectrum and can be expressed using S as $w = \exp(-S)$. In this work, we present normalized HR spectra, i.e., probability density functions (PDFs) of the corresponding electronic transition. By this definition, the area under the curve is one in all cases, and thus the DW factor is the area under the ZPL peak. We note that the temperature dependent width of ZPL emission is not incorporated in this theory and the long wavelength acoustic phonons are not sampled in our calculations due to the finite size of the supercell.

B. Charge transition levels

Formation energy as defined in Ref. [45] can be expressed for the $V_C V_{\text{Si}}$ defect as

$$E_{\text{form}}^q = E_{\text{tot}}^q - \frac{n_{\text{Si}} + n_{\text{C}}}{2}\mu_{\text{SiC}} + qE_{\text{F}} + \Delta V(q), \qquad (13)$$

where E_{tot}^q is the total energy of the defective system in the q charge state, $n_{\text{Si/C}}$ is the number of the Si/C atoms in the supercell, μ_{SiC} is the chemical potential of Si-C unit in the perfect 4H SiC crystal, E_{F} represents the Fermi level and $\Delta V(q)$ stands for the charge correction term. To determine

$\Delta V(q)$, we use the Freysoldt charge correction scheme [46]. For calculating the $(-/0)$ charge transition level referenced to the conduction band minimum (CBM) one may use the following formula:

$$E_{q+1/q}^{\mathrm{CBM}} = E_{\mathrm{CBM}} - E_{q+1/q}, \qquad (14)$$

where E_{CBM} is the CBM energy, and $E_{q+1/q}$ is the charge transition level calculated as

$$E_{q+1/q} = E_{\mathrm{tot}}^q - E_{\mathrm{tot}}^{q+1} + \Delta V(q) - \Delta V(q+1). \qquad (15)$$

By increasing the temperature, the charge transition levels may shift due to the thermal evolution of the band edges and the thermal shift of the vibrational free energy.

Effect of the thermal shift of the CBM manifests in Eq. (14), where E_{CBM} is in fact temperature dependent. Since E_{CBM} decreases upon increasing temperature [47], the $(-/0)$ charge transition level referenced to the CBM and hence the reionization threshold energy will also decrease upon introducing this correction as $E_{-/0}^{\mathrm{CBM}*} = E_{-/0}^{\mathrm{CBM}} - \Delta E^{\mathrm{CBM}}(T)$.

On the other hand, thermal shift of the charge transition levels originating from the vibrational entropy of the defect is governed by the temperature dependent vibrational free energy in the corresponding charge state (F^q) formulated as [48]

$$F^q(T) = \sum_i \left\{ \frac{1}{2}\hbar\omega_i + k_{\mathrm{B}}T\ln\left[1 - \exp\left(-\frac{\hbar\omega_i}{k_{\mathrm{B}}T}\right)\right] \right\}, \quad (16)$$

where $\hbar$ and k_{B} are the reduced Planck constant and Boltzmann constant, respectively, and ω_i is the frequency of the ith phonon mode. Since free energy contributes to the total energy of the system, the $E_{-/0}$ charge transition level shifts by the free energy difference of the negative and neutral charge states $[\Delta F(T)]$. The free energy difference is defined as $\Delta F(T) = F^-(T) - F^0(T)$, so the free energy-shifted charge transition level can be written as $E_{-/0}^{\mathrm{CBM}**} = E_{-/0}^{\mathrm{CBM}} + \Delta F(T)$. In order to calculate $\Delta F(T)$, we considered all the quasilocal phonon modes associated with the motion of the atoms within the second neighbor shells around the $V_C V_{\mathrm{Si}}$ defect both in the negative and neutral charge states.

Combining the two correction terms, the reionization energy threshold energy is defined as

$$E_{-/0}^{\mathrm{CBM}}(\mathrm{corr}) = E_{-/0}^{\mathrm{CBM}} - \Delta E^{\mathrm{CBM}}(T) + \Delta F(T). \qquad (17)$$

C. Computational methodology

In order to obtain the neutral PL spectra for all defect configurations, we calculated the neutral ground and optically accessible excited states by DFT. Excited state calculations were carried out by applying the ΔSCF method [49]. In addition, we calculated the ground state of $V_C V_{\mathrm{Si}}^-$ for the $V_C V_{\mathrm{Si}}^- \rightarrow V_C V_{\mathrm{Si}}^0$ reionization spectra. Nuclear coordinates of the global energy minimum in the initial and final electronic states, i.e., the fully relaxed geometries were obtained by minimizing the quantum mechanical forces between the ions falling below the threshold of 0.01 eV/Å. The corresponding electronic structure for all $V_C V_{\mathrm{Si}}^0$ defect configurations in the neutral ground/excited state and that for $V_C V_{\mathrm{Si}}^-$ in the ground state is shown in Fig. 2. Here we note that both excited state of $V_C V_{\mathrm{Si}}^0$ and ground state of $V_C V_{\mathrm{Si}}^-$ introduce a degenerate e
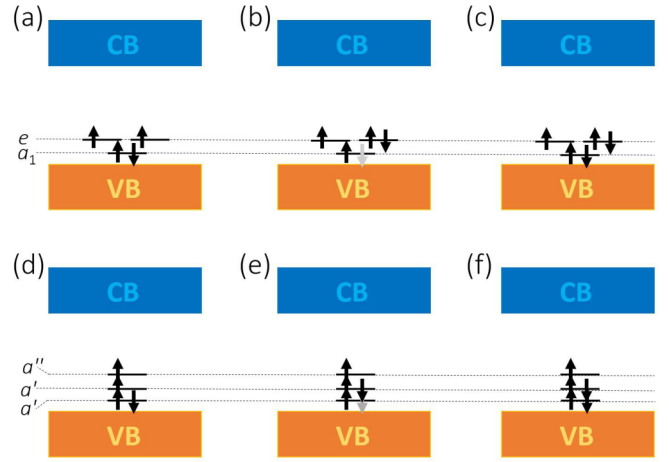
FIG. 2. Electronic structure of the [(a) and (d)] ground and [(b) and (e)] excited state of $V_C V_{\mathrm{Si}}^0$ defects, and [(c) and (f)] ground state of $V_C V_{\mathrm{Si}}^-$ defects. (a)–(c) corresponds to the axial defects exhibitng C_{3v} symmetry and those of (d)–(f) show the electronic structures of the basal defect configurations possessing C_{1h} symmetry. Black arrows represent electrons while gray arrows stand for the reminiscent holes after optical excitation. The valence band (VB) and conduction band (CB) of 4H SiC are also indicated along with the characters of the corresponding Kohn-Sham states.

KS state to the band gap occupied by three electrons giving rise to the so-called dynamical Jahn-Teller (JT) effect [50]. Accordingly, the symmetry will be reduced from C_{3v} to C_{1h} (even for axial configurations) by coupling to phonons in order to split the corresponding e level removing the degeneracy in total energy. In calculation of the corresponding spectra we use static JT distorted geometries exhibiting the lowest total energy.

All investigated $V_C V_{\mathrm{Si}}$ defect configurations were modelled in a 576-atom 4H supercell. In order to reach sufficient accuracy in the total energies, we employed Γ-point centered $2 \times 2 \times 2$ k-point mesh for all ground and excited state calculations. Here we note that only Γ-point sampling of the Brillouin zone fails to achieve sufficient accuracy manifesting in the incorrect order in the total energies of the different $V_C V_{\mathrm{Si}}$ configurations as pointed out in Ref. [34]. For the electronic structure calculations we employed the HSE06 range-separated hybrid functional [51]. Kohn-Sham (KS) wave functions were expanded in plane wave basis set with the cutoff energy of 420 eV. Only the valence electrons were treated explicitly, the core-electrons with ionic potentials were considered in the framework of projector augmented wave (PAW) method [52] as implemented in the Vienna *ab initio* simulation package (VASP) [53].

For the vibrational modes, we calculated the corresponding dynamical matrix containing the second order derivatives of the total energy by means of the Perdew-Burke-Ernzerhof (PBE) [54] functional. We also determined the corresponding eigenvectors. Here we note that the calculated dynamical matrix and hence the HR and DW factors depend on the supercell size where the former may be a bit underestimated because of neglect of long wavelength phonons.

TABLE I. Absorption cross-sections (σ_{th}) and ratios of the ZPL intensities (R_{th}) in the numerical PL spectrum for the individual $V_C V_{Si}^0$ configurations. We also report the ZPL ratios for the experimental nonquenched spectra recorded at $T = 3.5$ K (R_{exp}). We show values for both 976-nm and 1053-nm excitations.

	σ_{th}		R_{th}		R_{exp}	
Config.	976 nm	1053 nm	976 nm	1053 nm	976 nm	1053 nm
hh	0.0015	0.0013	1.00	1.00	1.00	1.00
kk	0.0018	0.0017	1.26	1.33	1.16	1.33
hk	0.0021	0.0019	1.42	1.42	2.62	2.55
kh	0.0022	0.0015	1.53	1.18	3.90	1.75

Localization of the phonon modes can be addressed by the inverse participation ratio (IPR) [41,55] defined as

$$\text{IPR}_k = \frac{N \sum_i \mathbf{u}_i^4}{\left(\sum \mathbf{u}_i^2\right)^2}, \qquad (18)$$

where $\mathbf{u}_i$ is the vector displacement amplitude of the ith atom in the kth phonon mode and N is the number of atoms in the defective supercell that is $N = 574$ in our case. Consequently, the IPR falls in the region of $[1, N]$ and it is equal to the number of atoms vibrating in the certain phonon mode.

III. RESULTS AND DISCUSSION

In Secs. III A–III C, we provide our numerical results for the $V_C V_{Si}^0$ PL spectra and the temperature dependent reionization spectra for the $V_C V_{Si}^- \rightarrow V_C V_{Si}^0$ transition for all $V_C V_{Si}$ defect configurations. We also discuss the charge state control and simultaneous qubit manipulation of $V_C V_{Si}^0$ in 4H SiC with comparing our novel experimental and simulation results in Sec. III D.

A. PL spectra of $V_C V_{Si}^0$ configurations

In order to verify the methodology for calculating the PL spectra [42,49], we first compare the total PL spectrum (i.e., including all contributions from the individual $V_C V_{Si}$ configurations) obtained from theory with the nonquenched $V_C V_{Si}^0$ spectrum reported in Sec. III D. The nonquenched PL spectra were recorded at $T = 3.5$ K with using two different excitation wavelengths, 976 and 1053 nm (cf. Fig. 10) along with a 532-nm repump laser in order to

maintain the neutral charge state (i.e., to avoid quenching). We note that our simulations correspond to the $T = 0$ K condition which is close to the experimental one. Excitation energies can be taken into account in the calculations by multiplying the obtained numerical spectra with the optical absorption cross-sections (σ) of the individual $V_C V_{Si}$ configurations, respectively, as $L^{EM}(E_{ex}, \hbar\omega) = \sigma(E_{ex}) L^{EM}(\hbar\omega)$, where $L^{EM}(E_{ex}, \hbar\omega)$ denotes the PL line shape upon the excitation energy of E_{ex}. In our calculations, we identified $\sigma(E_{ex})$ as the transition probability at E_{ex} in the absorption PDF, i.e. $\sigma(E_{ex}) = \text{PDF}_{abs}(E_{ex})$. We report the corresponding values in Table I.

The total numerical PL emission spectra (cf. Fig. 3) upon 976-nm and 1053-nm excitations are then obtained by adding up the PL spectra obtained for the individual $V_C V_{Si}$ configurations weighted by the relative strength of absorption probability (σ_{th}) at those excitation wavelengths. Numerical and experimental emission spectra can be well-compared via the ZPL intensities. To this end, we listed the ratios of the numerical and experimental ZPL intesities in Table I. We find that the trend in the ZPL intensity ratios agrees well; however, there are differences between the absolute values. This discrepancy may arise from the fact that, while polarization properties manifest in the experimental spectrum (i.e., the experimental spectrum is the sum of the individual polarization contributions parallel and perpendicular to the c axis), all the emitted photons are considered in the theoretical spectrum. This implies that optical alignment of the PL measurement plays a key role in the recorded line shape. In order to allow detection of both polarizations simultaneously, the experimental PL spectrum was registered through the edge of the sample as given in Sec. III D. Thus the origin of the discrepancy may be caused by other processes that are not considered in our model.

The calculated HR emission PDFs of $V_C V_{Si}^0$ configurations are shown in Fig. 4. ZPLs in all spectra are shifted to the experimental ZPL positions as reported in Table II. We note that the fluorescence spectra of $V_C V_{Si}^0$ hh and hk configurations have recently been computed in Ref. [57] reporting similar line shapes. Here we provide the PL lineshape for each configuration with high resolution in the PSB for further analysis. The IPR analysis of the phonons shows that phonon modes at $\approx$17–35 meV are mostly localized on the three Si atoms neighboring the V_C with the IPR of $\approx$1–5, while phonon modes at $\approx$35–115 meV region are mostly localized
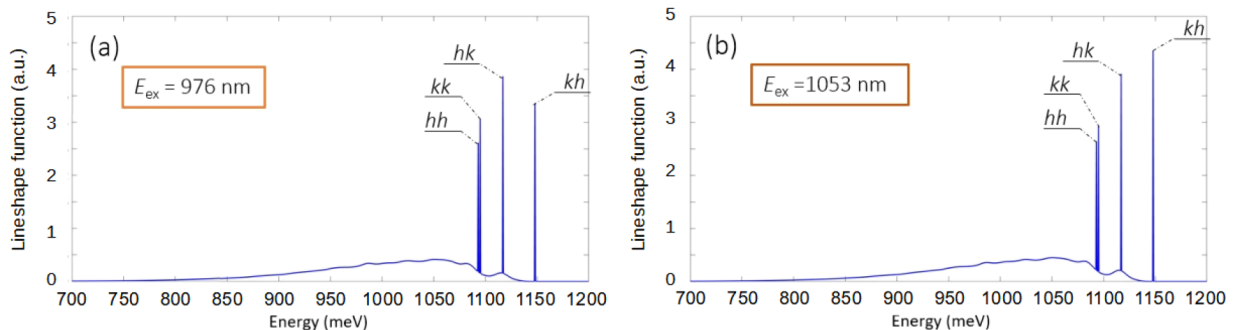
FIG. 3. Calculated PL spectra of divacancies in 4H SiC upon (a) 976-nm and (b) 1053-nm excitation wavelengths.
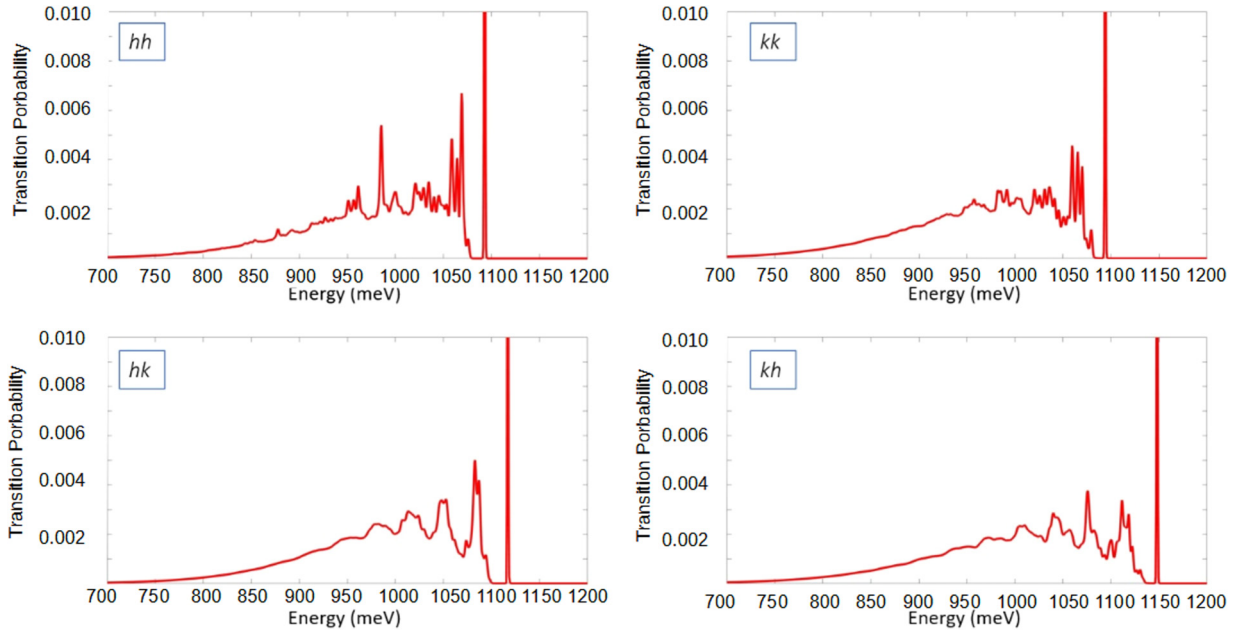
FIG. 4. Calculated Huang-Rhys emission spectrum for the optical transition of $V_{Si}V_C^0$ for all defect configurations (see the textbox) assuming resonant excitation. All the spectra are normalized, i.e., the area under the curves is one, hence, the y axis represents the electronic transition probability from the optically accessible excited state to the ground state.

on the three C atoms around the V_{Si} with a similar IPR range [Fig. 5(b)]. The sum of the individual PL spectra is shown in Fig. 5(a).

The corresponding HR and DW factors along with the experimental and calculated ZPLs are listed in Table II. The lowest ZPL energy corresponds to $V_C V_{Si}^0(hh)$ along with the smallest HR factor and thus the largest DW factor. Here we note that the exceptionally large DW factor of the $V_C V_{Si}^0(hh)$ was also found in a previous study [57]. Interestingly, ZPL energy of $V_C V_{Si}^0(kk)$ is extremely close to that of $V_C V_{Si}^0(hh)$, i.e., the difference between the experimental values is only 1 meV ($\approx 0.1\%$). On the other hand, $V_C V_{Si}^0(kk)$ exhibits by $\approx 19\%$ larger HR factor and $\approx 40\%$ lower DW factor than those of $V_C V_{Si}^0(hh)$. We note that the DW factor of $V_C V_{Si}^0(hh)$ is close to that of $V_C V_{Si}^0$ in the cubic 3C SiC (0.07) [58]. We already showed a counterintuitive issue on the example of vanadium defect in 4H SiC [10] that the hexagonal site in 4H SiC has a cubic-like environment in the second and third neighbor shells unlike the quasicubic site. Therefore hh configuration of divacancy in 4H SiC indeed shows similar properties to those of the divacancy in 3C SiC. The largest

TABLE II. Calculated and experimental (Ref. [56]) ZPLs for all $V_C V_{Si}^0$ defect configurations in 4H SiC. We apply the notations for the centers observed in experiments from Ref. [3]. The calculated Huang-Rhys (S) and Debye-Waller (w) factors are also listed.

Config. (Center)	E_{ZPL}^{exp} (eV)	E_{ZPL}^{calc} (eV)	S	w
hh (PL1)	1.095	1.142	2.856	0.057
kk (PL2)	1.096	1.151	3.380	0.034
hk (PL3)	1.119	1.167	3.428	0.032
kh (PL4)	1.150	1.187	3.540	0.029

ZPL energy and HR factor along with the lowest DW factor occur for $V_C V_{Si}^0(kh)$ in 4H SiC.

B. Temperature dependent reionization spectra from phonon-assisted transitions

We conclude that the HR theory $V_C V_{Si}^0$ reproduces well the experimental spectrum, therefore we can apply this theory for understanding the temperature dependent reionization process. Ionization energy of point defects can be approximated by their charge transition level which is the position of the Fermi level in the band gap for which the formation energies of the defect in the two charge states are equal. We showed in our previous study [34] that the energy separation between the $(+/0)$ level and the valence band maximum (VBM) is at $E_{+/0}^{VBM} \approx 1.1$ eV, which is smaller than that between the $(0/-)$ level and the CBM at $E_{-/0}^{CBM} \approx 1.2$–1.3 eV for all $V_C V_{Si}$ configurations in 4H SiC at $T = 0$ K. Therefore we concluded that the dark state of the divacancy is $V_C V_{Si}^-$, i.e., the singly negative charge state of the defect, into which $V_C V_{Si}^0$ is converted upon photoexcitation below the reionization threshold energy because the photon energy of the applied laser used to illuminate $V_C V_{Si}^0$ (> 1.1 eV) could immediately convert $V_C V_{Si}^+$ into $V_C V_{Si}^0$ with ejecting a hole in the valence band. The experimental threshold energies recorded at cryogenic temperatures and the calculated charge transition levels are listed in Table III.

The reionization threshold energies can depend on the temperature that we divided to three contributors: (i) phonon-assisted photoionization, (ii) entropy contribution to the charge transition levels, and (iii) temperature shifts of the band edges of the host crystal.

First, we consider here the phonon-assisted photoionization process. As we are interested in the threshold energy,
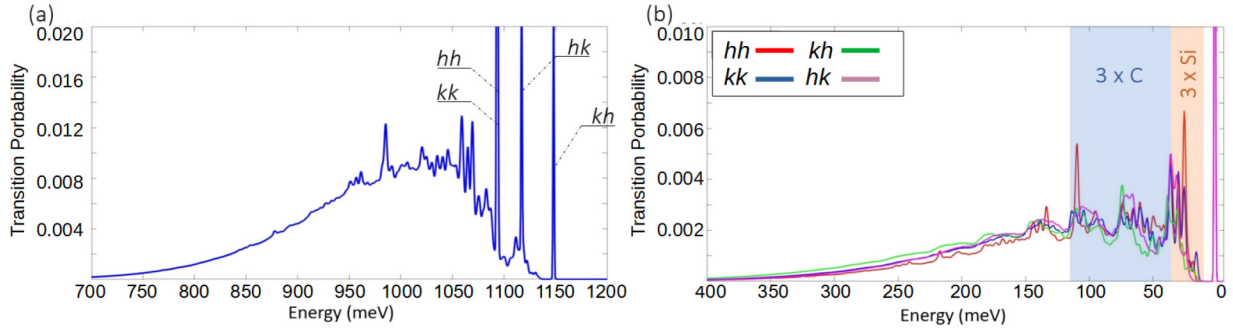
FIG. 5. (a) Probability density function (PDF) of the $V_C V_{Si}^0$ defects in 4H SiC related to (a) total and (b) individual PL spectra. The total spectrum is generated by adding up the individual PDFs of $V_C V_{Si}^0$ configurations. ZPL energies are shifted to 0 meV, in order to read the phonon energy. Localization of phonon modes is indicated by shaded area in (b) caused by the three Si atoms around the V_C (yellow shaded area) and by the three C atoms around V_{Si} (blue shaded area).

we consider only the CBM and the phonon-assisted optical transition to CBM which is technically well represesented in our simulation in terms of folding the M-point of the Brillouin-zone to the Γ point of the supercell. The calculated reionization threshold energy, i.e., the $E_{0/-}^{CBM}$ in the particular case of divacancies in 4H SiC, can be considered as an absorption of the electron from the highest occupied defect level by the CBM states which corresponds to a no-phonon process. At elevated temperatures, the vibronic excited states of $V_C V_{Si}^-$ may be occupied which effectively lowers the threshold energy to reach CBM compared to that of the no-phonon process. This is analogous to the ZPL energy versus phonon sideband related energies in the absorption process, so HR absorption spectrum calculations were applied for all $V_C V_{Si}$ configurations as shown in Fig. 6. We used the $V_C V_{Si}^0$ phonons for calculating the phonon sideband of the reionization spectra as we did for the PL spectra (see Sec. III A).

In Fig. 6, the ZPL peak corresponds to the no-phonon ionization energies and coincides with the adiabatic $E_{0/-}^{CBM}$ charge transition levels. By raising the temperature, peaks and broad features appear at lower energies than the ZPL energy which are responsible to lower the reionization threshold energies. There are some subtle differences between in the low-energy PSB spectrum of the different configurations, e.g., sharp features are visible for hh and hk configurations at $T = 600$ K, while those for kk and kh configurations almost completely disappear. This implies a stronger electron-phonon coupling in the reionization process for configurations with $V_C(h)$

which are associated with the vibration of the three nearest neighbor Si atoms. The HR and DW factors of the absorption (reionization) spectra for each configuration are listed in Table III, which characterize the general strength of the electron-phonon coupling associated with the optical transition.

The calculation of the phonon-assisted reionization process can be expressed as $E_{rei} = E_{ex} \pm E_{ph}$, where E_{ex} represents the applied photoexcitation energy and E_{ph} stands for the energy of the absorbed ($-$) or emitted ($+$) phonon. The former process will reduce the threshold energy for reionization. At croygenic temperatures close to $T = 0$ K, the no-phonon process is dominating for the threshold energy of reionization, i.e., $E_{ex}^{min} = E_{rei}$ as listed in Table III. At elevated temperatures, Fig. 6 clearly shows that, indeed, the threshold energy for reionization may be reduced but the absorption cross-section has an exponential tail in the low-energy PSB of the optical transition. However, it is difficult to define the exact condition at which absorption cross-section the reionization process is observable in experiments. In order to quantify the theoretical description of this process, we setup a condition in which we assume that the reionization process is definitely observable when the total reionization cross-section mediated by the phonons at a given temperature is at least as large as the integrated reionization cross-section associated with the half of the DW factor of the reionization spectrum which corresponds to the reionization cross-section at cryogenic (close to $T = 0$ K) temperatures.

Since the calculated reionization spectra are normalized (those are PDFs), exciting with the energy of E_{ex} results in the total transition probability, i.e., the cumulative transition probability (CTP) of

$$\text{CTP}(E_{ex}) = \int_0^{E_{ex}} \text{PDF}(\varepsilon) d\varepsilon, \qquad (19)$$

where ε is the variable for the excitation energy in the reionization spectra. At cryogenic temperatures, we assume that $\text{CTP}(E_{rei} = E_{ZPL}) = w/2$ with assuming symmetrical broadening of the ZPL peak of the reionization spectrum. By increasing the temperature, the phonon excited states of the negative divacancy are occupied according to the Bose-Einstein function, thus the effective reionization energy decreases which results in a lower threshold energy of photoionization. In other words, the phonon-assisted

TABLE III. Experimental threshold energies of photoionization recorded at cryogenic temperatures (Ref. [34]) which is approximated by the $(0/-)$ charge transition levels for all $V_C V_{Si}$ configurations referenced to the CBM. The corresponding HR (S) and DW (w) factors are also provided which are related to the phonon assisted ionization process.

Center	Config.	E_{rei} (eV)	$E_{0/-}^{CBM}$ (eV)	S	w
PL1	hh	1.310	1.245	2.691	0.068
PL2	kk	1.310	1.209	3.038	0.048
PL3	hk	1.321	1.307	2.490	0.083
PL4	kh	1.281	1.174	3.267	0.038

FIG. 6. Calculated temperature dependent transition probability density functions for HR absorption spectrum of $V_C V_{Si}^- \rightarrow V_C V_{Si}^0$ transition for the four configurations as indicated in the text boxes at 0 K (black lines), 150 (red lines), 300 (blue lines), 450 (green lines) and 600 K (magenta lines). The ZPL energies—associated with the reionization energies at cryogenic temperature—were shifted to the experimental data recorded at cryogenic temperatures (Ref. [34] as listed in Table III).

photoionization results in $\text{PDF}(\varepsilon) > 0$ for $\varepsilon < E_{ZPL}$ energy. One can find the threshold reionization energy at a given temperature for each configuration for which the reionization probability is equal to that of at $T = 0$ K, i.e., $\text{PDF}(\varepsilon) = w/2$ is fulfilled.

We calculated the $\text{CTP}(\varepsilon)$ at temperatures of $T = 0, 150, 300, 450$ and , 600 K for each divacancy configuration in 4H SiC that we depict for (hh) configuration in Fig. 7. $\text{CTP}(\varepsilon)$ can be read out as shaded area under the curves in Fig. 7(a), whereas it is a line plot in Fig. 7(b). $\text{CTP}(\varepsilon)$ at all investigated temperatures is similar to the lineshape of the cumulative distribution function of the Boltzmann distribution. The wavy line shapes around the ZPL energy visible for low-temperature simulations could be an artifact by neglecting the temperature broadening of the ZPL emission and other size effects of the supercell approach.

We also indicated E_{ex}^{min} at each temperature in Fig. 7(a) and depicted for all $V_C V_{Si}$ configurations at $T = 0, \dots, 600$ K in 50 K steps in Fig. 8(a). This approach results in a plateau up to $T \approx 150$–200 K for $E_{ex}^{min}(T)$, and it then drops for all the $V_C V_{Si}$ configurations at higher temperatures. In other words, $E_{ph}^{min}(T)$ is about zero in our approximation for $T < 150$–200 K, and it increases for $T > 150$–200 K. In order to gain further insight to the temperature dependence of the phonon threshold energy, $E_{ph}^{min}(T)$, we employed the Boltzmann distribution [$f(\varepsilon, T)$] as the low concentration limit of the Bose-Einstein distribution for the phonon bath appearing in the region of $[0, E_{rei}]$ as

$$f(\varepsilon, T) = \frac{1}{kT} \exp\left(\frac{\varepsilon - E_{rei}}{kT}\right), \quad (20)$$

where $k = 8.617 \times 10^{-5}$ eV/K is the Boltzmann constant. By setting the value of the integral to $w/2$ in the region of $[0, E_{rei}]$, we arrive at

$$\int_0^{E_{ex}^{min}} \frac{1}{kT} \exp\left(\frac{\varepsilon - E_{rei}}{kT}\right) d\varepsilon = \frac{w}{2}. \quad (21)$$

By evaluating the integral of Eq. (21) and rearranging the equation, we arrive at

$$E_{ph}^{min}(T) = -\ln\left[\frac{w}{2} + \exp\left(-\frac{E_{rei}}{kT}\right)\right] kT. \quad (22)$$

Since the values of E_{rei} are around 1300 meV the typical values of $\exp(-\frac{E_{rei}}{kT})$ is about 10^{-12} at the given temperature range, and hence negligible next to the calculated DW values of $w/2 \approx 0.03$–0.09 (see Table III). Finally, $E_{ph}^{min}(T)$ can be approximated as

$$E_{ph}^{min}(T) \approx -\ln\left(\frac{w}{2}\right) kT \quad (23)$$

yielding linear characteristics for $E_{ph}^{min}(T)$ with the slope of $m = -\ln(w/2)k$. Furthermore, since $w/2 < 1$, $E_{ph}^{min}(T)$ increases with T within this approximation. As a result, reionization threshold energy can be expressed as

$$E_{ex}^{min}(T) = E_{rei} - E_{ph}^{min}(T) \approx E_{rei} + \ln\left(\frac{w}{2}\right) kT. \quad (24)$$

Linear behavior of $E_{ex}^{min}(T)$ is indeed manifested in our simulations plotted in Fig. 8(a), for $T > 200$ K. This approach
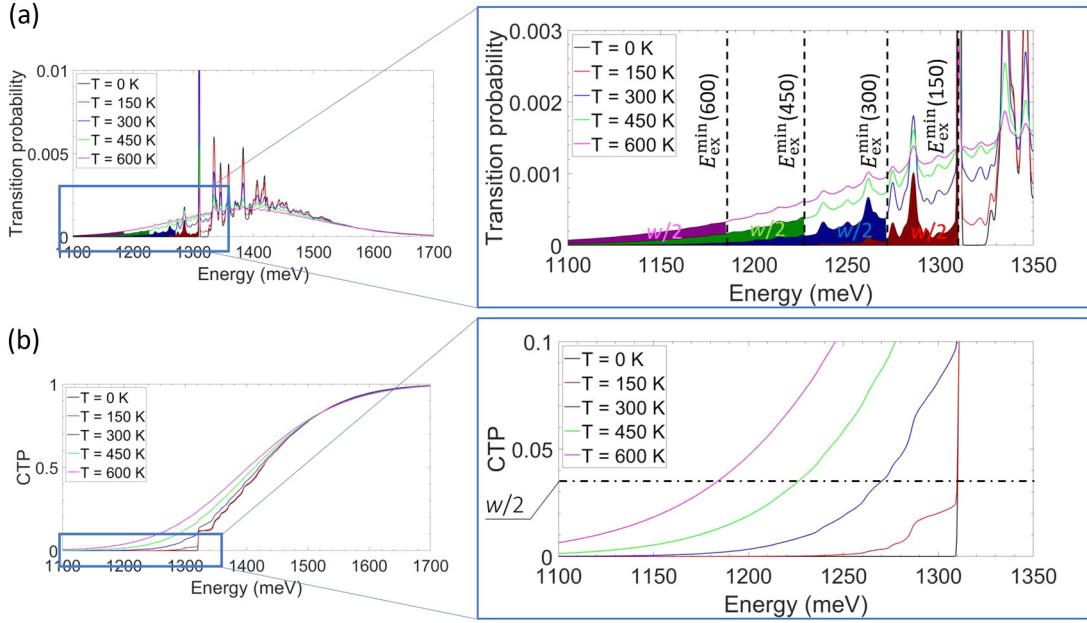
FIG. 7. (a) Numerical temperature dependent transition probability density functions of the HR absorption (reionization) spectra for the $V_C V_{Si}^-(hh) \rightarrow V_C V_{Si}^0(hh)$ transition. PSB below the ZPLs given rise at elevated temperatures are enlarged and the corresponding reionization threshold energies (E_{ex}^{min}) are indicated by vertical dashed lines, whereas the cumulative transition probability (CTP) of $w/2$ are represented by shaded areas. (b) CTP for the $V_C V_{Si}^-(hh) \rightarrow V_C V_{Si}^0(hh)$ transition. Half of the DW factor, i.e., $w/2$ is indicated in the expanded part of the CTP.

predicts that $E_{rei}(T = 300\,\text{K})$ reaches 1250–1320 meV (990–940 nm) for $V_C V_{Si}$ configurations in 4H SiC which is close to the typical photoexcitation energy of the neutral divacancies in 4H SiC. We note that Eq. (24) is valid for any point defects and their PL spectrum within the employed approximations by substituting E_{rei} with the corresponding ZPL energy of (re)ionization. We emphasize that the actual phonon-assisted reionization may be observed for ε with $\text{PDF}(\varepsilon) < w/2$ depending on the integration time and other factors in the experiments that are discussed in Sec. III D. Furthermore, the temperature shifts of the charge transition level and the band edges, i.e., temperature dependence of E_{rei}, should be also taken into for understanding temperature dependence of the reionization process.

C. Temperature dependent reionization thershold energies including contributions from entropy and temperature shifts of the conduction band minimum

Temperature dependence of the charge transition levels of point defects was discussed in Sec. II B which depends on the entropy effects in the formation enthalpy of the point defects in their charge states ($\Delta F(T)$) and the electron-phonon renormalization of the band edges. Thermal evolution of the band edges in 4H SiC was already determined in a previous study [47]. According to this work, thermal shifts of the VBM and CBM becomes noticeable at around $T = 300\,\text{K}$, where the CBM/VBM is decreased/increased by $\approx 5\,\text{meV}$, respectively, with respect to their $T = 0\,\text{K}$ value. In Table IV, we provide the values for $\Delta F(T)$ and $E_{-/0}^{CBM}(\text{corr})$ for all $V_C V_{Si}$ defect configurations at room-temperature.

We find that the ΔF is one order magnitude lower for the kk and hk configurations than those for the hh and kh configurations. Since $F^q(T)$ depends on frequency of the phonon modes [cf. Eq. (16)], ω_i, this trend may arise from the stronger distortion between the neutral and negative charge states for the hh and kh configurations than that for the kk and hk configurations. Indeed, the geometry distortion is larger by about 10% for the hh and kh configurations than that for kk and hk configurations. As a result, correction in $E_{-/0}^{CBM}$ (cf. Table III) for the kk and hk configurations is tiny and further reduces the reionization threshold energies. On the other hand, the free energy contribution rather inceases the reionization threshold energies for hh and kh configurations and mostly compensates the thermal shift of the band edge [cf. Figs. 8(b) and 8(c)]. These results clearly demonstrate that considering only the free energy term in the temperature dependence of the photoionization threshold energies can lead to a false result as the contribution from the phonon-assisted ionization process could dominate and even change the sign of the thermal shift in the ionization threshold energy [cf. Figs. 8(a) and 8(c)].

TABLE IV. Free energy correction term (ΔF) to $E_{-/0}^{CBM}$ and the corrected charge transition levels referenced to the CBM [$E_{-/0}^{CBM}(\text{corr})$] at room temperature ($T = 300\,\text{K}$). We already included the $\Delta E_{CBM}(T) = 5\,\text{meV}$ decrease of the CBM in the calculation of $E_{-/0}^{CBM}(\text{corr})$.

Config.	hh	kk	hk	kh
ΔF(eV)	0.041	−0.008	−0.001	0.050
$E_{-/0}^{CBM}$(corr) (eV)	1.281	1.196	1.301	1.219
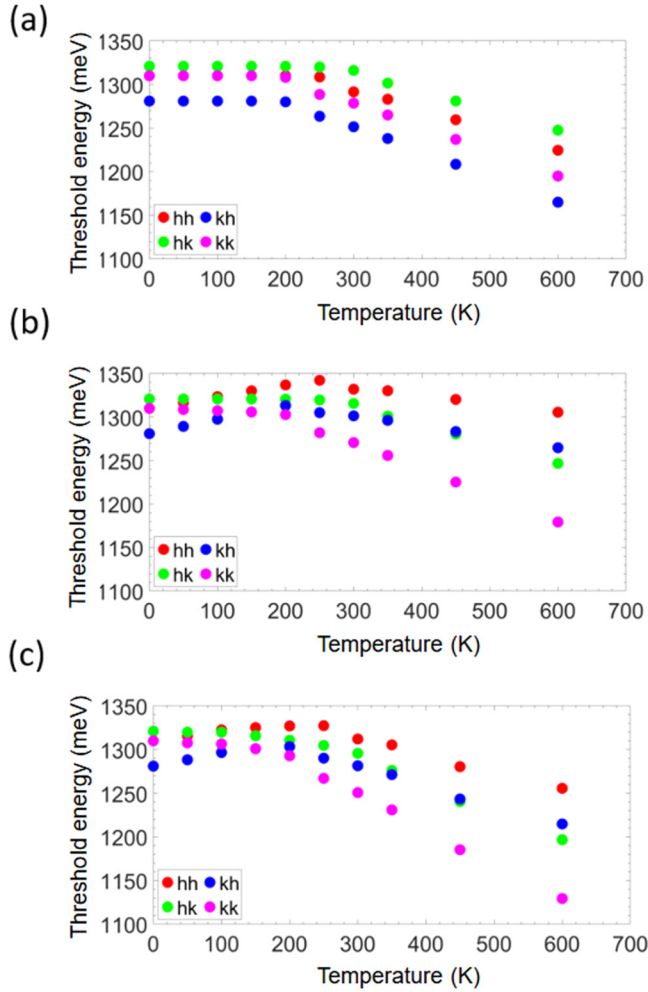
FIG. 8. Reionization threshold energies $[E_{ex}^{min}(T)]$ (a) without thermal corrections on the charge transition levels, (b) corrected with $\Delta F(T)$ and (c) corrected further with $\Delta E^{CBM}(T)$ as a function of temperature for all $V_C V_{Si}$ defect configurations.

D. Experimental aspects

The above consideration shows that the quenching behavior of the divacancy in all configurations is distinctly different at low temperature (say <2 K) and at elevated temperatures. While at low temperature there is a distinct threshold for the excitation energy for each divacancy configuration, below which quenching of the corresponding PL is observed but can be recovered using higher-energy repump illumination. Above the threshold the PL of the corresponding divacancy configuration does not quench even if no repump is applied. At higher temperatures, however, there are no distinct thresholds because phonon-assisted photoionization of the $V_C V_{Si}^-$ charge state becomes possible, whereas no phonons are available at low temperature for this process. Given a fixed excitation energy E_{ex}, the minimum energy of a phonon E_{ph}^{min} that can combine with the incident photon to produce phonon-assisted photoionization of $V_C V_{Si}^-$ is given by the energy balance quoted in Sec. III A,

$$E_{rei} = E_{ex} + E_{ph}^{min}. \tag{25}$$

Here we assume that $E_{ex} < E_{rei}$, hence $E_{ph}^{min} > 0$. All phonons with energies $E_{ph} > E_{ph}^{min}$ also contribute to phonon-assisted photoionization, hence the cumulative transition probability $CTP(E_{ex})$ is given by Eq. (19). From practical point of view, it may be desirable to have the possibility for optical charge state control also at elevated temperatures. This can be achieved by using lower excitation energies E_{ex}, because these provide lower $CTP(E_{ex})$, hence the quenching behavior can be preserved also at elevated temperatures. It is clear that if $E_{ph}^{min} \gg k_B T$ for given temperature T (the case of lower energy E_{ex}) the amount of phonons available for phonon-assisted reionization is negligible and $CTP(E_{ex}) \approx 0$. Note that E_{ex} is bound from below by the condition $E_{ex} > E_{ex}^{ZPL}$, where E_{ex}^{ZPL} refers to the corresponding divacancy configuration. Our goal here is to examine the concept of phonon-assisted reionization by comparing the quenching properties at higher temperatures for two excitation energies, both below the thresholds, but one of which is close to the threshold while the other is far enough so that $E_{ph}^{min} = E_{rei} - E_{ex} \gg k_B T$.

The energy diagram (inset in Fig. 9) depicts the two excitation cases for $E_{ex} = 1.270$ eV (976 nm) and $E_{ex} = 1.177$ eV (1053 nm), which have been used in the experiments presented below. Both excitations are below the thresholds for all divacancy configurations, but the former is close to the thresholds (only ≈ 11 meV lower than the threshold for PL4, cf. Table II), whereas the 1.177-eV excitation is about 100 meV (up to 140 meV for the different configurations) below all thresholds. As a consequence, the condition $E_{ph}^{min} \gg k_B T$ is fulfilled only for the second excitation at 1.177 eV, as long as the temperature does not exceed room temperature. The CTPs as a function of temperature for the two used excitations and for the four divacancy configurations are calculated using Eq. (19) and displayed in Fig. 9 in the temperature range 0–350 K. Using these dependencies we can make qualitative comparison with the experimental data presented in Fig. 10 and obtained using these two fixed laser excitations, 976 and 1053 nm. The repump laser beam used in these experiments is at 532 nm directed unfocused on the sample with power density of the order of 1 mW/cm^{-2}. On the other hand, the excitation beam (976 or 1053 nm) is moderately focused on the sample to a spot of ~1 mm diameter, with estimated power density at the sample of the order of several watts per cm^{-2}. The experimental conditions are detailed in Ref. [34].

We compare now the quenching behavior of the divacancy emission at different temperatures when the two different excitations are used. The experimental spectra obtained at different temperatures are presented in Fig. 10. The spectra with the infrared laser excitation alone (976 or 1053 nm) are obtained after switching off the repump laser and quenching the divacancy PL for about 1/2 hour, and are referred to further as the "quenched" spectra (denoted by Q in Fig. 10). The rest of the spectra are with the repump laser applied in addition to the infrared excitation; under these conditions the divacancy PL is stable and the spectra are denoted by NQ for "nonquenched" in Fig. 10. One can see from the spectra that at liquid He temperature (3.5 K) the divacancy PL quenches about 10–30 times for each of the two excitations, as expected because both excitation energies are below the thresholds for all divacancy configurations. Also, at this temperature essentially no
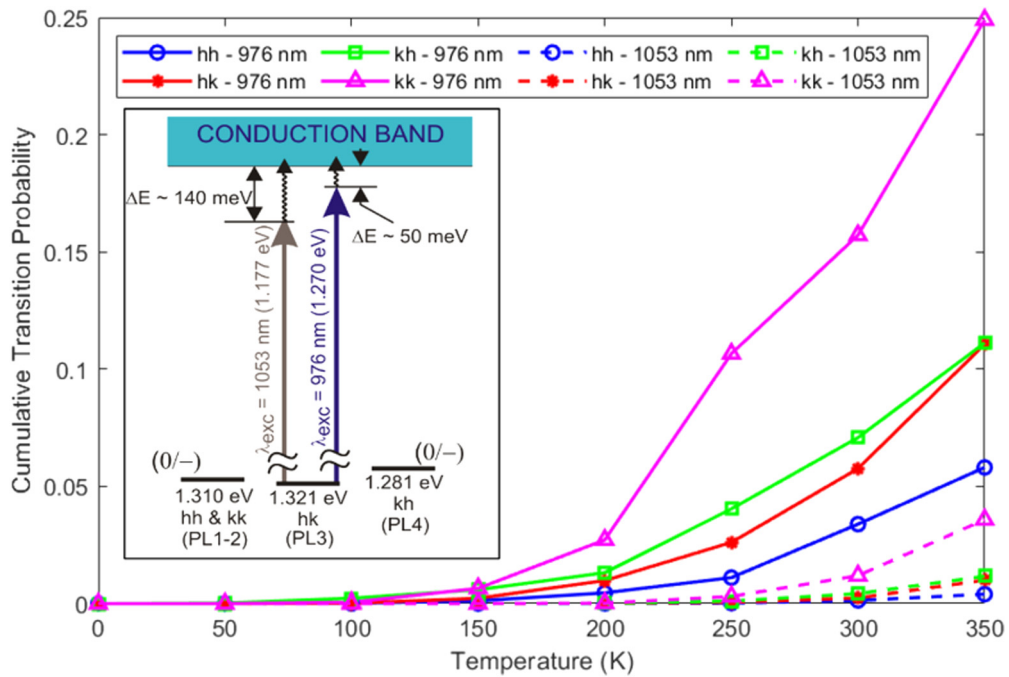
FIG. 9. Theoretical dependencies of the cumulative transition probability on the temperature for the four divacancy configurations as denoted for each curve taking all the temperature effects into account, and for the two excitation wavelengths used in the experiment. The inset displays an energy diagram of the phonon-assisted photoionization illustrated on the hk divacancy configuration. The (0/−) charge transition levels are labeled with the corresponding configuration and the experimentally determined energy separation from the conduction band. The two bold vertical arrows represent the two experimental laser energies whereas the wavy arrows represent the phonons with minimum energies needed for reionization of the divacancy from negative to neutral charge state.

phonons are available for phonon-assisted reionization, hence the accumulation of the divacancy in the negative charge state is irreversible for both IR excitations used. We notice also that in the particular sample used in these experiments the quenched PL never reaches zero intensity, similar to sample 1 of Ref. [34].

At 80 K, however, we notice differences in the quenching behavior of one of the divacancy configurations (*kh*). Namely, with the 976-nm excitation the PL4 line corresponding to the *kh* configuration shows nearly the same intensity in the quenched spectrum as in the "nonquenched", i.e., it does not quench. We notice here that the relative contribution of the PL4 line in the spectra at 80 K is strongly reduced compared to the spectra at 3.5 K, but this behavior is not understood at present. The rest of the lines (PL1–PL3) do quench exhibiting large intensity contrast (similar to that at 3.5 K) between the quenched and nonquenched spectra for both excitations. We notice further that the PL4 also quenches in a way similar to that at 3.5 K if the 1053-nm excitation is used. Referring to the CTP plots in Fig. 9 we notice that at temperature $T = 80$ K only the *kh* configuration (corresponding to the PL4 line) exhibits CTP ≈ 0.0015 for 976-nm excitation, while for the rest of the divacancy configurations at 976 nm and all configurations at 1053 nm the CTP is essentially negligible ($< 3.5 \times 10^{-4}$) for both excitation wavelengths. Thus the experimental data for the PL4 line imply that for CTP of only 0.0015 (0.15% probability of phonon-assisted ionization of $V_C V_{Si}^-$) the reionization process outcompetes the accumulation of the divacancy in the negative charge state. Consequently, for CTPs in the low 10^{-3} range one may expect to notice impact

of the phonon-assisted reionization on the quenching process. This provides a means to define semiquantitatively the experimental conditions when the rate of the phonon assisted reionization is comparable with the rate of capture of electrons to neutral divacancies, thus creating negatively charged ones. We can define that this condition (similar rates of ionization an reionization) is true if the quenched spectra exhibit roughly 50% of the intensity of the nonquenched ones.

At temperatures higher than 80 K, the contribution of the *kh* configuration (PL4 line and phonon sideband) in the spectrum can be neglected owing to the abovementioned rapid decrease of the PL4 intensity with increasing temperature. Thus we investigate the behavior of the PL1–PL3 lines, the phonon sidebands of which coalesce into a broad band extending between 1100 and 1320 nm. Note that also the threshold energies of these three configurations (*hk*, *hh*, and *kk*) are rather close according to the energy diagram inset in Fig. 9. At $T = 150$ K, the contributions from the these three divacancy configurations are still discernible via their zero-phonon lines, although the latter are much broader and weaker than at cryogenic temperature. However, the dominant contribution to the spectrum at this and higher temperatures comes from the PSBs of each configuration, which overlap to form a single band concealing the individual contribution from the different configurations. Therefore, in the following, we shall compare the intensities of the broad bands in the quenched and nonquenched spectra, looking for each infared (IR) excitation for the temperature when the intensity in the quenched spectrum is roughly half of the intensity in the nonquenched one.
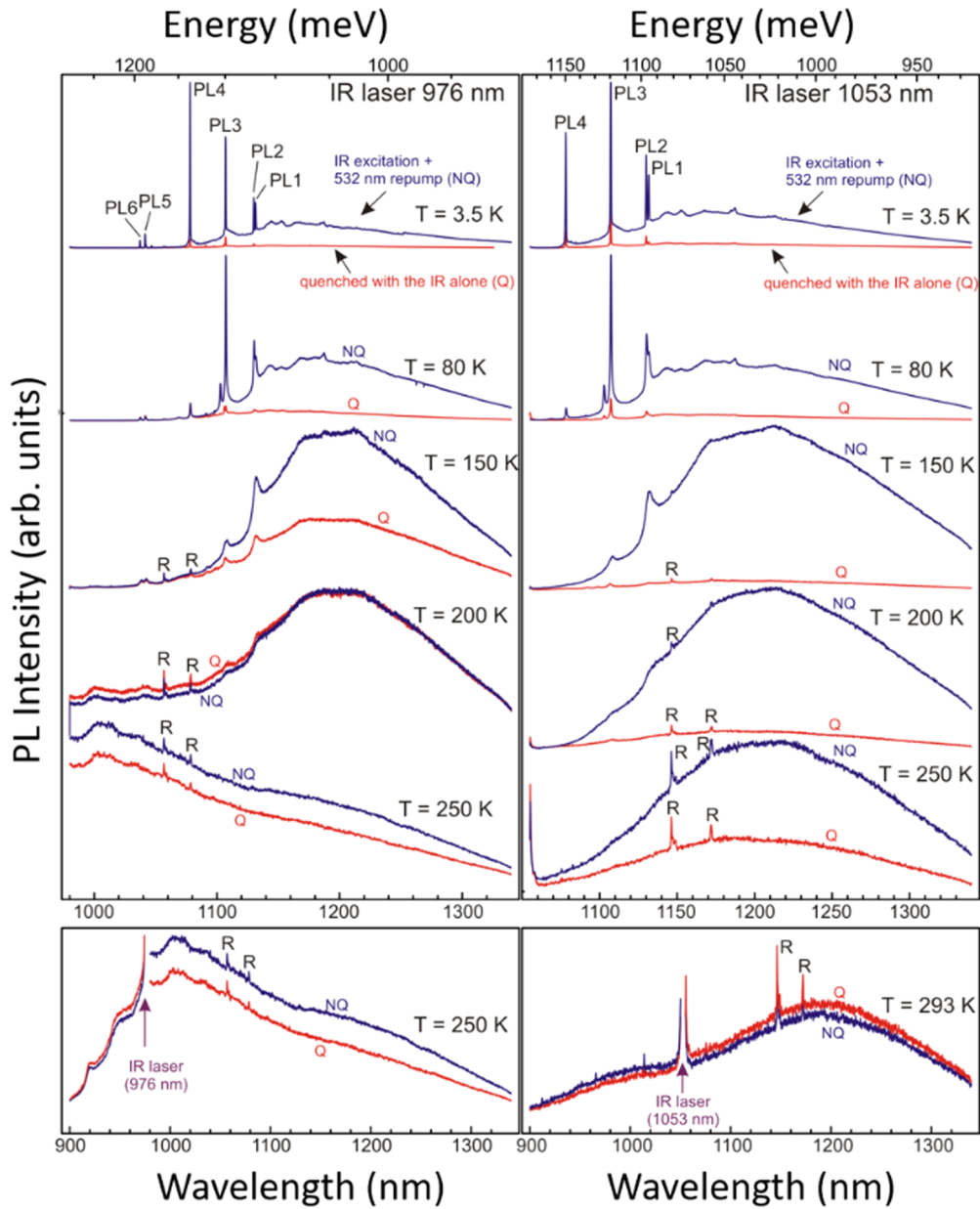
FIG. 10. Experimental spectra of the divacancy emission obtained at different temperatures with the simultaneous application of the IR laser and the 532-nm repump laser (denoted NQ, or nonquenched) and with the IR laser alone after a long term quenching (Q, or quenched). The panels to the left (right) refer to the 976 nm (1053 nm) IR laser, respectively. The two bottom panels show also the anti-Stokes part of the spectra and illustrate the upconversion in the emission of the silicon vacancy.

We observe from Fig. 10 that our criterion is fulfilled for the 976-nm excitation at $T = 150$ K, when the intensity of the phonon sideband is about $1/2$ of the intensity in the nonquenched one. The corresponding CPTs for the 976-nm excitation are 2.3×10^{-3}, 1.2×10^{-3}, and 6.5×10^{-3} for the hk, hh, and kk configurations, respectively. These values are in good agreement with our anticipation that the phonon-assisted reionization rate is comparable with that of the divacancy ionization to $V_C V_{Si}^-$. Further temperature increase to 200 K completely inhibits the quenching as seen from the corresponding spectrum for 976 nm excitation in Fig. 10. On the other hand, the quenching is well pronounced for the 1053 nm excitation at both temperatures, 150 and 200 K. For this excitation (1053 nm), one notices significant

change in the quenching contrast only at 250 K, when the intensity of the quenched spectrum is about 30% of that of the nonquenched one. The corresponding theoretical CPTs are 1.2×10^{-4}, 4.4×10^{-4}, and 3.1×10^{-3} for the hk, hh, and kk configurations, respectively. These values imply that kk configuration contributes the most or entirely to the nonquenched spectrum, and we still expect impact on the quenching properties for such values of the CPT for hk and hh configurations. Thus the experimental data are in reasonable agreement with the theory and we may conclude that the dominant reason for the loss of the quenching properties above $T = 150$ K quoted in Ref. [34] where 976-nm excitation has been used is the phonon-assisted reionization activated at this and higher temperatures. In contrast, the quenching property disappears

completely only at room temperature when the 1053 nm excitation is used. Indeed, the CPT values in these conditions are 2.4×10^{-3}, 1.3×10^{-3}, and 1.2×10^{-2} for the hk, hh, and kk configurations, respectively, which are all above the quoted CPT threshold value.

We notice the appearance of the luminescence of the silicon vacancy (V_{Si}^-) at elevated temperatures when the 976-nm excitation is used, via the upconversion mechanism discussed in Ref. [34]. Indeed, at $T = 250$ K the spectrum obtained with 976-nm excitation is dominated by the contribution of V_{Si}^-, as shown in the bottom left panel of Fig. 10. However, the V_{Si}^- spectrum can be discerned even below $T = 200$ K when 976-nm excitation is used. For instance, the Stokes part of the V_{Si}^- luminescence is clearly visible in the spectrum at $T = 200$ K (left panels). In contrast, weak contribution from the upconverted V_{Si}^- luminescence can be observed with 1053-nm excitation only at room temperature (293 K, bottom right panel); at $T = 250$ K or lower temperatures its contribution to the spectrum is negligible and the dominant luminescence is that of the divacancy. Since the upconverted V_{Si}^- luminescence is associated with increased generation of free electrons [34], its appearance serves as an indicator of the rapid increase of the free-electron population with temperature when 976-nm is used, owing to the rapid increase of the CTP with increasing temperature for this excitation. On the contrary, the increase in the CTP (and the electron population) is much smaller with the 1053-nm excitation, so that the contrast between quenched and nonquenched spectra disappears only at $T = 293$ K and is associated with the weak appearance of upconverted luminescence from V_{Si}^-, as expected.

Thus the experimental data suggest that the phonon-assisted divacancy reionization apparently influences the quenching behavior at temperatures and excitations for which the CTP is of the order of low 10^{-3}, i.e., well below 1%. We notice that this value is much smaller than the half of the Debye-Waller factor ($w/2$) used as a reference during the discussion of the probabilities in the previous section. We can understand the fact that low reionization probability (of the order of 0.1%) is sufficient to counteract the process of accumulation of the divacancy in the negative charge state, if we consider the model describing the quenching dynamics presented in Ref. [34]. In this simplest model, two types of centers are considered: traps capable to emit electrons to the conduction band as a result of photoionization (via the IR excitation) and divacancies capable of capturing electrons. Consequently, the traps can be in two states: with captured electron (capable to emitted an electron to the conduction band via photoionization), and with a missing electron (capable to recapture of free electron). The divacancies in this model are also assumed to have two charge states: neutral (capable of capturing electron) and negatively charged (with captured electron). The latter state cannot be photoionized using IR excitation below the threshold, hence the accumulation of divacancies in the negative charge state leads to quenching of the luminescence from the neutral charge state.

Naturally, there exist various traps capable of emitting electrons via photoionization, for instance, the nitrogen donors, the carbon vacancy, the silicon vacancy in double ($2-$) and triple ($3-$) negative charge states, just to name a few. The model in Ref. [34] assumes only one kind of traps which may be thought as having the dominant capture cross section for electrons and the dominant concentration. If these were the nitrogen donors, for instance, then the capture cross-section of ionized donors for electrons is "giant" [59] owing to the possibility for capture via the excited donor states. On the other hand capturing of electrons occurs to the neutral divacancy which, therefore, is assumed to have much smaller capture cross section for electrons. Indeed, in order to reproduce correctly the shape of the time decay of the divacancy PL, the model in Ref. [34] admits that the ratio of capture cross sections for electrons of the divacancy and the trap is 2×10^{-3}. In other words, an electron is emitted from traps and recaptured from traps many times before it eventually can be captured by the divacancy. On the other hand, one can assume that the probability for absorption of a photon which is stipulated by the optical-absorption cross-section is similar for the traps and the divacancies. Recapturing of electrons is fast to the traps, but only about 0.1% of the total free-electron population are captured to divacancies. Thus the divacancy population in the negative charge state grows slowly, and this slow process can be counteracted by phonon-assisted reionization with a CTP of about 0.1%.

To conclude this section, we can state that excitations with longer wavelength (lower energy) widen the temperature range in which the quenching phenomenon can be observed. However, in many cases when the silicon vacancy V_{Si}^- is also present, excitation with too high photon energies (e.g., close to or even above the threshold of all divacancy configurations) leads at elevated temperatures to upconverted PL of V_{Si}^- instead of excitation of the divacancy PL, as illustrated in the low left panel of Fig. 10. Thus, if the PL of the divacancy is to be measured at higher temperatures or at room temperature, lower excitation energies are also preferable. It should be noted, however, that it might be possible to stabilize the divacancy PL by Fermi-level tuning even when excitations above the thresholds is applied, but this is a subject of a different study and will not be discussed here.

IV. CONCLUSIONS

In this paper, we investigated the photoluminescence line shape of the $V_C V_{Si}^0$ qubits in 4H SiC at $T = 0$ K by DFT calculations. We obtained the corresponding PL spectra by using the HR theory and found that the corresponding PSB exhibits a rich set of sharp features for each configuration. The sharp features originate from quasilocalized phonon modes. We showed via IPR analysis that phonons are localized on the three neighbor Si atoms around the V_C in the phonon energy region of ≈ 17–35 meV, while those falling in the ≈ 35–115 meV are localized on the three neighbor C atoms around the V_{Si}. We also calculated the HR and DW factors of the PL spectra yielding the smallest HR factor (and thus the largest DW factor) for $V_C V_{Si}^0(hh)$ implying $V_C V_{Si}^0(hh)$ to be the most attractive $V_C V_{Si}^0$ qubit candidate in terms of extracting the brightest optical transition at the coherent ZPL emission among the divacancy configurations in 4H SiC. These optical properties of $V_C V_{Si}^0(hh)$ in 4H SiC are reminescent of the $V_C V_{Si}^0$ in the cubic polytype of SiC, i.e., 3C SiC.

We carried out experiments and *ab initio* calculations on the temperature dependent $V_C V_{Si}^- \rightarrow V_C V_{Si}^0$ reionization

process in 4H SiC. We found that the reionization of divacancies in 4H SiC upon unfocused green repump laser illumination is a complex process in which very efficient traps (most likely nitrogen donors) and the silicon vacancy defects present in the sample are involved. For efficient driving of divacancy qubits in 4H SiC at elevated temperatures, lower excitation energies are preferable. We found that the PL signals of divacancies can be fully recovered at room temperature with typical infrared photoexcitation energies without applying any green repump laser for such divacancy configurations which have stable fluorescence up to room temperature. This result strongly indicates that the reionization threshold energies of divacancies decrease with increasing temperature. Our calculations revealed that not the thermal shifts of the band edges nor the charge transition levels of divacancies caused by entropy contributions to the formation enthalpy are responsible for an effective lowering of the reionization threshold energies at elevated temperatures but rather the activation of phonon-assisted photoionization transitions. This result highlights a general conclusion that phonon-assisted photoionization processes should be always considered in understanding the thermally activated photoionization of point defects in semiconductors and insulators.

ACKNOWLEDGMENTS

[1] M. W. Doherty, N. B. Manson, P. Delaney, F. Jelezko, J. Wrachtrup, and L. Hollenberg, Phys. Rep. **528**, 1 (2013).

[2] A. Gali, Nanophotonics **8**, 1907 (2019).

[3] W. F. Koehl, B. B. Buckley, F. J. Heremans, G. Calusine, and D. D. Awschalom, Nature (London) **479**, 84 (2011).

[4] S. Castelletto, B. C. Johnson, V. Ivády, N. Stavrias, U. T., A. Gali, and T. Oshima, Nat. Mater. **13**, 151 (2014).

[5] D. J. Christle, A. L. Falk, P. Andrich, P. V. Klimov, J. Ul Hassan, N. T. Son, E. Janzén, T. Ohshima, and D. D. Awschalom, Nat. Mater. **14**, 160 (2015).

[6] M. Widmann, S.-Y. Lee, T. Rendler, N. T. Son, H. Fedder, S. Paik, L.-P. Yang, N. Zhao, S. Yang, I. Booker, A. Denisenko, M. Jamali, S. A. Momenzadeh, I. Gerhardt, T. Ohshima, A. Gali, E. Janzén, and J. Wrachtrup, Nat. Mater. **14**, 164 (2015).

[7] G. Wolfowicz, C. P. Anderson, B. Diler, O. G. Poluektov, F. J. Heremans, and D. D. Awschalom, Sci. Adv. **6**, eaaz1192 (2020).

[8] A. Lohrmann, N. Iwamoto, Z. Bodrog, S. Castelletto, T. Ohshima, T. J. Karle, A. Gali, S. Prawer, J. C. McCallum, and B. C. Johnson, Nat. Commun. **6**, 7783 (2015).

[9] M. Radulaski, M. Widmann, M. Niethammer, J. L. Zhang, S.-Y. Lee, T. Rendler, K. G. Lagoudakis, N. T. Son, E. Janzén, T. Ohshima, J. Wrachtrup, and J. Vučković, Nano Lett. **17**, 1782 (2017).

[10] L. Spindlberger, A. Csóré, G. Thiering, S. Putz, R. Karhu, J. U. Hassan, N. T. Son, T. Fromherz, A. Gali, and M. Trupke, Phys. Rev. Appl. **12**, 014015 (2019).

[11] R. Nagy, M. Niethammer, M. Widmann, Y.-C. Chen, P. Udvarhelyi, C. Bonato, J. U. Hassan, R. Karhu, I. G. Ivanov, N. T. Son, J. R. Maze, T. Ohshima, O. O. Soykal, A. Gali, S.-Y. Lee, F. Kaiser, and J. Wrachtrup, Nat. Commun. **10**, 1954 (2019).

[12] C. Babin, R. Stöhr, N. Morioka, T. Linkewitz, T. Steidl, R. Wörnle, D. Liu, E. Hesselmeier, V. Vorobyov, A. Denisenko, M. Hentschel, C. Gobert, P. Berwian, G. V. Astakhov, W. Knolle, S. Majety, P. Saha, M. Radulaski, N. T. Son, J. Ul-Hassan *et al.*, Nat. Mater. **21**, 67 (2022).

[13] S.-Y. Lee, M. Niethammer, and J. Wrachtrup, Phys. Rev. B **92**, 115201 (2015).

[14] H. Kraus, V. A. Soltamov, F. Fuchs, D. Simin, A. Sperlich, P. G. Baranov, G. V. Astakhov, and V. Dyakonov, Sci. Rep. **4**, 5303 (2014).

[15] D. Simin, V. A. Soltamov, A. V. Poshakinskiy, A. N. Anisimov, R. A. Babunts, D. O. Tolmachev, E. N. Mokhov, M. Trupke, S. A. Tarasenko, A. Sperlich, P. G. Baranov, V. Dyakonov, and G. V. Astakhov, Phys. Rev. X **6**, 031014 (2016).

[16] D. Simin, F. Fuchs, H. Kraus, A. Sperlich, P. G. Baranov, G. V. Astakhov, and V. Dyakonov, Phys. Rev. Appl. **4**, 014009 (2015).

[17] M. Niethammer, M. Widmann, S.-Y. Lee, P. Stenberg, O. Kordina, T. Ohshima, N. T. Son, E. Janzén, and J. Wrachtrup, Phys. Rev. Appl. **6**, 034001 (2016).

[18] C. J. Cochrane, J. Blacksberg, M. A. Anders, and P. M. Lenahan, Sci. Rep. **6**, 37077 (2016).

[19] A. N. Anisimov, D. Simin, V. A. Soltamov, S. P. Lebedev, P. G. Baranov, G. V. Astakhov, and V. Dyakonov, Sci. Rep. **6**, 33301 (2016).

[20] A. Gali, Phys. Status Solidi (b) **248**, 1337 (2011).

[21] B. Magnusson and E. Janzén, Mater. Sci. Forum **483-485**, 341 (2005).

[22] P. G. Baranov, I. V. Il'in, E. N. Mokhov, M. V. Muzafarova, S. B. Orlinskii, and J. Schmidt, J. Exp. Theor. Phys. Lett. **82**, 441 (2005).

[23] N. T. Son, P. Carlsson, J. ul Hassan, E. Janzén, T. Umeda, J. Isoya, A. Gali, M. Bockstedte, N. Morishita, T. Ohshima, and H. Itoh, Phys. Rev. Lett. **96**, 055501 (2006).

[24] B. Somogyi and A. Gali, J. Phys.: Condens. Matter **26**, 143202 (2014).

[25] B. Somogyi, V. Zolyomi, and A. Gali, Nanoscale **4**, 7720 (2012).

[26] D. Beke, J. Valenta, G. Károlyházy, S. Lenk, Z. Czigány, B. G. Márkus, K. Kamarás, F. Simon, and A. Gali, J. Phys. Chem. Lett. **11**, 1675 (2020).

[27] D. J. Christle, P. V. Klimov, C. F. de las Casas, K. Szász, V. Ivády, V. Jokubavicius, J. Ul Hassan, M. Syväjärvi, W. F. Koehl, T. Ohshima, N. T. Son, E. Janzén, A. Gali, and D. D. Awschalom, Phys. Rev. X **7**, 021046 (2017).

[28] A. Bourassa, C. P. Anderson, K. C. Miao, M. Onizhuk, H. Ma, A. L. Crook, H. Abe, J. Ul-Hassan, T. Ohshima, N. T. Son, G. Galli, and D. D. Awschalom, Nat. Mater. **19**, 1319 (2020).

[29] A. L. Falk, P. V. Klimov, B. B. Buckley, V. Ivády, I. A. Abrikosov, G. Calusine, W. F. Koehl, A. Gali, and D. D. Awschalom, Phys. Rev. Lett. **112**, 187601 (2014).

[30] G. Wolfowicz, F. J. Heremans, C. P. Anderson, S. Kanai, H. Seo, A. Gali, G. Galli, and D. D. Awschalom, Nat. Rev. Mater. **6**, 906 (2021).

[31] A. Gali, M. Bockstedte, N. T. Son, T. Umeda, J. Isoya, and E. Janzén, in *Silicon Carbide and Related Materials 2005*, Materials Science Forum Vol. 527 (Trans Tech Publications Ltd, 2006), pp. 523–526

[32] A. Gali, J. Mater. Res. **27**, 897 (2012).

[33] L. Gordon, A. Janotti, and C. G. Van de Walle, Phys. Rev. B **92**, 045208 (2015).

[34] B. Magnusson, N. T. Son, A. Csóré, A. Gällström, T. Ohshima, A. Gali, and I. G. Ivanov, Phys. Rev. B **98**, 195202 (2018).

[35] C. P. Anderson, A. Bourassa, K. C. Miao, G. Wolfowicz, P. J. Mintun, A. L. Crook, H. Abe, J. Ul Hassan, N. T. Son, T. Ohshima, and D. D. Awschalom, Science **366**, 1225 (2019).

[36] O. Zwier, D. O'Shea, A. R. Onur, and C. H. van der Wal, Sci. Rep. **5**, 10931 (2015).

[37] G. Wolfowicz, C. P. Anderson, A. L. Yeats, S. J. Whiteley, J. Niklas, O. G. Poluektov, F. J. Heremans, and D. D. Awschalom, Nat. Commun. **8**, 1876 (2017).

[38] D. A. Golter and C. W. Lai, Sci. Rep. **7**, 13406 (2017).

[39] P. Siyushev, H. Pinto, M. Vörös, A. Gali, F. Jelezko, and J. Wrachtrup, Phys. Rev. Lett. **110**, 167402 (2013).

[40] K. Huang, A. Rhys, and N. F. Mott, Proc. R. Soc. London A **204**, 406 (1950).

[41] A. Alkauskas, B. B. Buckley, D. D. Awschalom, and C. G. V. de Walle, New J. Phys. **16**, 073026 (2014).

[42] A. Gali, D. T., M. Vörös, G. Thiering, E. Cannuccia, and A. Marini, Nat. Commun. **7**, 11327 (2016).

[43] P. Debye, Ann. Phys. **348**, 49 (1913).

[44] I. Waller, Z. Phys. **17**, 398 (1923).

[45] A. Csóré, N. T. Son, and A. Gali, Phys. Rev. B **104**, 035207 (2021).

[46] C. Freysoldt, J. Neugebauer, and C. G. Van de Walle, Phys. Rev. Lett. **102**, 016402 (2009).

[47] E. Cannuccia and A. Gali, Phys. Rev. Materials **4**, 014601 (2020).

[48] D. Wickramaratne, C. E. Dreyer, B. Monserrat, J.-X. Shen, J. L. Lyons, A. Alkauskas, and C. G. Van de Walle, Appl. Phys. Lett. **113**, 192106 (2018).

[49] A. Gali, E. Janzén, P. Deák, G. Kresse, and E. Kaxiras, Phys. Rev. Lett. **103**, 186404 (2009).

[50] I. B. Bersuker, *The Jahn-Teller Effect* (Cambridge University Press, 2006).

[51] J. Heyd, G. E. Scuseria, and M. Ernzerhof, J. Chem. Phys. **118**, 8207 (2003).

[52] P. E. Blöchl, Phys. Rev. B **50**, 17953 (1994).

[53] G. Kresse and J. Furthmüller, Phys. Rev. B **54**, 11169 (1996).

[54] J. P. Perdew, K. Burke, and M. Ernzerhof, Phys. Rev. Lett. **77**, 3865 (1996).

[55] R. J. Bell, P. Dean, and D. C. Hibbins-Butler, J. Phys. C **3**, 2111 (1970).

[56] A. L. Falk, B. B. Buckley, G. Calusine, W. F. Koehl, V. V. Dobrovitski, A. Politi, C. A. Zorman, P. X.-L. Feng, and D. D. Awschalom, Nat. Commun. **4**, 1819 (2013).

[57] A. Hashemi, C. Linderälv, A. V. Krasheninnikov, T. Ala-Nissila, P. Erhart, and H.-P. Komsa, Phys. Rev. B **103**, 125203 (2021).

[58] A. Csóré, N. Mukesh, G. Károlyházy, D. Beke, and A. Gali, J. Appl. Phys. **131**, 071102 (2022).

[59] M. Lax, Phys. Rev. **119**, 1502 (1960).